

# Electromagnetic Scattering From Randomly-Centered Parallel Single-Walled Carbon Nanotubes Embedded in a Dielectric Slab

Ahmed M. Hassan, *Member, IEEE*, and Edward J. Garboczi

**Abstract**—An analytical full wave model of parallel, randomly centered carbon nanotubes (CNTs) embedded in a dielectric slab was developed to calculate the electromagnetic scattering from CNT composites. The model simulates empty and metal-filled single walled CNTs as infinitesimally thin wires, parallel and infinitely long in the  $z$  direction, but randomly located in the  $x$ - $y$  plane. The wires have the equivalent impedance of CNTs and are embedded in a dielectric slab with finite thickness in the  $x$  direction but infinite in the  $y$  and  $z$  directions. The electromagnetic radiation propagates in the  $x$  direction, and the entire model is periodic in the  $y$  direction. The main goal of this work is to investigate how the variations in the random locations and impedances of the CNTs can lead to variations in the electromagnetic scattering from the composite. Composites with metal-filled CNTs exhibit more variations in the electromagnetic scattering than unfilled CNTs. The model also showed that increasing the density of CNTs, decreasing the losses of the dielectric matrix, and the random incorporation of nonidentical CNTs increases the variations in the electromagnetic scattering. The model is finally used to demonstrate how simple fabrication tolerances can affect the variations in electromagnetic scattering.

**Index Terms**—Carbon nanotubes (CNTs), electromagnetic interaction, microwave propagation, nanocomposites, terahertz (THz).

## I. INTRODUCTION

SINCE the early 1990s, carbon nanotubes (CNTs) have been one of the most interesting additives for the fabrication of composites with unique properties [1]. CNTs are seamless graphene layers rolled into tubes with specific folding configurations and angles, termed chirality [1]. CNTs exhibit exceptional mechanical and electrical properties due to their extremely large aspect ratio as well as the  $sp^2$  orbital carbon bonds in the walls of the tubes. CNT composites have been incorporated in many electromagnetic applications such as antennas [2]. The properties of CNT composites are highly sensitive to the radius, length, and the chirality of the CNT additive, the density (i.e., loading) of the CNTs in the composite, the spatial distribution of the CNTs, and the interaction of the

CNT with the embedding matrix [3]. Electromagnetic waves could be usefully employed for the nondestructive evaluation of the previous properties of CNT composites. However, to interpret such electromagnetic measurements, it is necessary to model the interactions of electromagnetic waves with CNT composites. In all the following text, CNT is taken to mean single-walled CNT only.

Modeling the electromagnetic scattering from CNT composites in the microwave and terahertz range, which is the focus of this work, has received much attention in the last decade [4]–[11]. The electromagnetic models developed for scattering from CNT can be divided into two dimensional (2-D) [4]–[6] and three dimensional (3-D) models [7]–[11].

In 2-D models, the CNTs are modeled as infinitely long thin wires with no variation in the axial direction whereas in 3-D models, the finite length of the CNT is explicitly taken into account. In 2-D models, Mikki *et al.* calculated the full wave electromagnetic scattering from single-wall CNTs using a modal expansion [4]. The basis of the model was to use the cylindrical symmetry of the single-wall CNTs to expand the scattered fields into an infinite series of Bessel and Hankel functions and apply suitable boundary conditions at the SWCNT wall [4]. Using a similar approach, Berres *et al.* calculated the electromagnetic scattering from infinitely long empty and gold-filled MWCNT [5]. Nefedov studied the electromagnetic modes guided by multiple parallel CNTs [6], which were assumed to be infinitely long and embedded in the uniform medium of air. The CNTs were arranged in uniform hexagonal or rectangular unit cells that were repeated periodically in one direction in the plane and were finite in the other in-plane direction [6].

In practice, 2-D models are valid when the lengths of the CNT are significantly larger than the wavelength (i.e., 10 times the wavelength [5]). Typical lengths of ultra-long CNT are of the order of a few millimeters, and can reach lengths as long as 550 mm [12]. For a 10-mm-long CNT, a 2-D model will be relatively accurate for frequencies higher than 300 GHz [5]. In addition, even for CNTs with smaller length or for lower frequencies, 2-D models can give qualitative insight into the fundamental properties of CNT composites at a much lower computational expense than 3-D models [5].

For 3-D models, the finite length of the CNT is explicitly modeled. Hanson explored the transmitting properties of a dipole antenna consisting of a single metallic CNT using the classical Hallén's type integral equation [7]. CNTs are not perfectly conducting since they have a finite surface conductivity and, therefore, the tangential electric fields do not necessarily

Manuscript received April 16, 2014; revised June 17, 2014; accepted July 20, 2014. Date of publication July 25, 2014; date of current version October 02, 2014. This work was supported in part under the National Institute of Standards and Technology project, "Carbon Nanocomposite Manufacturing: Processing, Properties, Performance."

The authors are with the Materials and Structural Systems Division, Engineering Laboratory, National Institute of Standards and Technology, Gaithersburg, MD 20899 USA (e-mail: amh@nist.gov; edward.garboczi@nist.gov).

Color versions of one or more of the figures in this paper are available online at <http://ieeexplore.ieee.org>.

Digital Object Identifier 10.1109/TAP.2014.2343240

vanish at the CNT wall. To account for this finite conductivity, a nonzero term was added to the classical Hallén's integral equation to account for the distributed impedance per unit length of the CNT [7]. The distributed impedance per unit length is defined as the ratio between the electric field and the total axial current flowing alongside the wall of the CNT [13]. The method of moments (MOM) was then used to solve Hallén's integral equation to calculate the current distribution on the CNT [7].

Hallén's integral equation was extended to simulate infinite [8], [9] and finite [11] arrays of aligned finite-length metallic carbon nanotubes in free space. In the finite array, the current on each CNT in the array is solved for explicitly using the MOM [11]. This increases the computational requirements of the model significantly, which limits the number of CNTs and the number of frequencies that can be considered [11].

The goal of this paper is to examine the effect of random geometry and material properties on the microwave and terahertz scattering from a 2-D model of CNTs embedded in a dielectric (e.g., epoxy) matrix using an analytically exact full wave approach. The model combines the features of the models discussed earlier, and the novelty in this work is the embedding of the CNTs in a solid matrix, not just free space, and the randomness in their spatial locations. The CNTs are modelled as infinitely long parallel wires that are randomly arranged in a unit cell that is repeated periodically, as shown in Fig. 1. The dielectric slab has a finite thickness in the  $x$ -direction, is infinite in the  $z$  direction with its  $x$  interfaces parallel to the axis of the CNTs, and is periodic in the  $y$ -direction. All multiple reflections between the CNTs and the dielectric slab are analytically incorporated. Even though the model developed herein is 2-D, as was defined earlier, the innovation in this work is that it quantitatively investigates how varying the random CNT locations affects electromagnetic scattering. It also quantifies the effect of various parameters on these variations in the electromagnetic scattering: the frequency, the CNT weight fraction in the composite, the filling material inside the CNTs, and the electrical properties of the dielectric slab. Since the model is analytically solved, as opposed to using finite element or finite difference techniques, the effect of random geometry and material parameters can be thoroughly explored in a reasonable computational time.

Some preliminary results on ordered CNT arrangements were published as conference proceedings [14]. However, the current work extends the modeling to partially random CNT composites as well as significantly expanding the parametric study of the electromagnetic scattering from composites with different geometrical and electrical properties.

## II. CNT CONDUCTIVITY AND DISTRIBUTED IMPEDANCE

The axial surface conductivity,  $\sigma_{\text{cnt}}$ , of a CNT, as a function of angular frequency  $\omega$ , was derived by Slepyan *et al.*, using the semiclassical Boltzmann transport equation, as follows [15]:

$$\sigma_{\text{cnt}} \cong -j \frac{2e^2 v_F}{\pi^2 \hbar b (\omega - j\nu)} \quad (1)$$

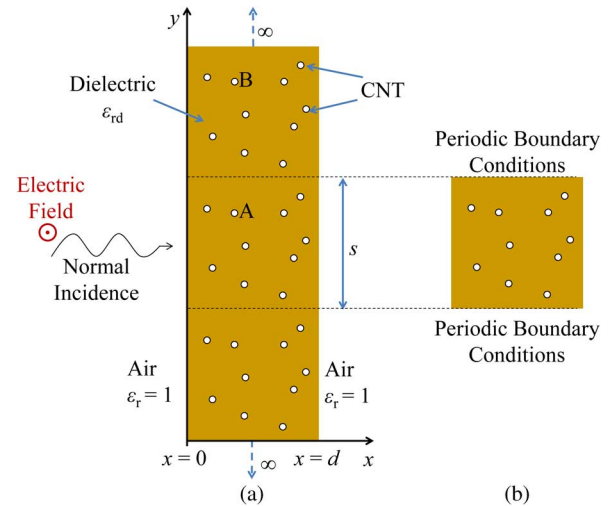


Fig. 1. (a) CNT composite modeled as a dielectric slab with finite thickness,  $d$ , in the  $x$  direction, with infinitely long aligned (in the  $z$ -direction) CNTs modeled as embedded wires; (b)  $x - y$  plane unit cell of the CNT composite. The CNT radii are enlarged in the figure for clarity.

where  $e$  is the electron charge,  $v_F$  is the Fermi velocity,  $\hbar$  is the normalized Plank's constant,  $b$  is the CNT radius,  $\nu$  is the relaxation frequency, and  $j$  is the square root of  $-1$ . The Fermi velocity  $v_F$  can be expressed as  $v_F = (3\gamma_0 b_0)/(2\hbar)$ , where  $\gamma_0$  is the overlap integral (units of energy) and  $b_0$  is the graphene lattice spacing. The axial surface conductivity in (1) is only valid in the microwave and terahertz range for metallic CNT with small chirality indices  $(n, m) < 50$  [4]–[11]. The accuracy of (1) was validated using several experimental measurements [8]–[10], [16]. The parameters  $\nu$  and  $\gamma_0$  are used as free parameters to fit the experimental measurements with the model in (1). In this work, the following values  $\gamma_0 = 2.7$  eV and  $\nu = 3.33 \times 10^{11}$  rad/s were used similar to [6].

Following the approximate approach developed by Hanson [7], the distributed impedance, or impedance per unit length,  $Z_{\text{cnt}}^{\text{empty}}$ , of a CNT with a vacuum core can be defined as

$$Z_{\text{cnt}}^{\text{empty}} = \frac{1}{2\pi b \sigma_{\text{cnt}}} \Omega/\text{m}. \quad (2)$$

The axial surface conductivity in (1) and the distributed impedance in (2) were derived for empty or unfilled CNTs. However, the cores of CNTs are typically filled, either unintentionally during fabrication or intentionally to enhance their properties. Grimes *et al.* measured the electrical properties of as-fabricated and annealed CNT [18]. The annealing improved the crystallinity of the CNT as well as removing the iron carbide impurities incorporated in the CNTs during fabrication. Even though only approximately 7% of the mass was removed as iron impurities, the conductivity of the CNT dropped by a factor of three in the 75–1875 MHz range [18]. Moreover, CNT properties can be further enhanced by intentionally filling their cores with different materials such as metals or semiconductors [19]. The distributed impedance along the axis of metallic filled CNT can be approximated as the parallel impedance of

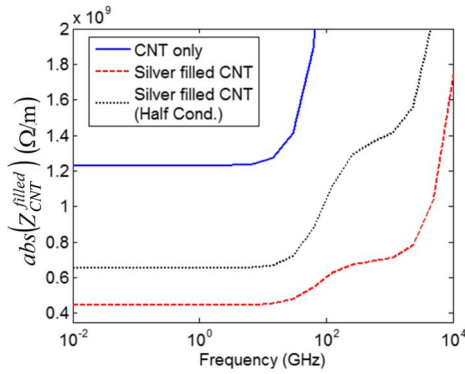


Fig. 2. Distributed impedance of empty and silver filled CNT. In the case of silver filled CNT, two conductivity values are used: 1) bulk conductivity and 2) half the bulk conductivity of silver.

an empty CNT and the metallic filling, modeled as a solid cylinder, as

$$Z_{\text{cnt}}^{\text{filled}} = \frac{Z_{\text{metal}} Z_{\text{cnt}}^{\text{empty}}}{Z_{\text{metal}} + Z_{\text{cnt}}^{\text{empty}}} \Omega/\text{m} \quad (3)$$

where

$$Z_{\text{metal}} = \frac{\gamma J_0(\gamma b)}{2\pi b \sigma_{3d} J_1(\gamma b)} \Omega/\text{m} \quad (4a)$$

$$\gamma = \sqrt{\frac{1}{2} \omega \mu_0 \sigma_{3d} (1 - j)} \text{m}^{-1}. \quad (4b)$$

In (3) and (4),  $Z_{\text{cnt}}^{\text{filled}}$  is the effective distributed impedance of the metallic filled CNT;  $Z_{\text{metal}}$  is the distributed impedance of a solid metallic cylinder which fills the CNT core [17];  $\gamma$  is the complex propagation factor in the bulk metal of the filling;  $\sigma_{3d}$  is the bulk conductivity of the metal;  $J_0$  and  $J_1$  are the zero order and first order Bessel functions, respectively; and  $\mu_0$  is the magnetic permeability in free space.

The effective distributed impedances of empty and silver filled (40, 40) armchair CNT are shown as the blue solid line and red dashed line in Fig. 2, respectively. In Fig. 2, the Drude model parameters reported in [20] are used to estimate the bulk conductivity,  $\sigma_{3d}$ , for silver. However, at nanoscale dimensions the conductivity of metals often drops below their bulk values due to scattering of the conduction electrons from the surface of the metals and from grain boundaries [17]. The exact drop in the conductivity from the bulk value depends on the dimensions of the metallic nanoparticles and the mean free path of the electrons but is difficult to determine exactly. Therefore, a third case is added to Fig. 2 as a dotted black line. In this case, the CNT is filled with silver but with conductivity equal to half of the bulk value to show the effect of decreasing the conductivity of the filling material on the distributed impedance. This case will be termed *half\_silver* filled in the rest of this paper.

For empty CNTs, the distributed impedance increases at frequencies higher than approximately 50 GHz. Filling the CNT with silver causes the effective distributed impedance to decrease to lower values at all frequencies. Also, in the case of silver filled CNT, the effective distributed impedance maintains these lower values over a higher frequency range in comparison

to the empty CNT, because the relaxation frequency of silver is higher than that of CNT.

If the impedance  $Z_{\text{cnt}}^{\text{filled}}$  is replaced with the distributed impedance of another inclusion, the model can be easily adapted to simulate different composites. For example, if  $Z_{\text{cnt}}^{\text{filled}}$  is replaced with the distributed impedance of carbon fibers the model can be easily adapted to calculate the reflected power from unidirectional continuous carbon fiber composites similar to those reported in [21].

### III. RANDOM WIRE GRID MODEL INSIDE A DIELECTRIC SLAB

Building on previous work, we now bring in randomness and model a CNT composite as randomly-centered periodic wire arrays embedded in a dielectric slab, as shown in Fig. 1(a), where each wire has the distributed impedance  $Z_{\text{cnt}}^{\text{filled}}$  defined in (3) above. All the CNT in each unit cell are aligned parallel to the  $z$ -axis and randomly positioned in the plane within the dielectric slab. The unit cell, shown in Fig. 1(b), has  $N$  randomly dispersed CNTs. The unit cell is then periodically repeated in the  $y$  direction with period  $s$ . The dielectric slab, with a relative dielectric permittivity  $\epsilon_{rd}$ , is infinite in the  $yz$  plane between  $0 < x < d$ . The regions  $x < 0$  and  $x > d$  are assumed to be free space with a relative dielectric permittivity of unity. The main assumption is that the radius of each CNT, termed  $b$ , is much smaller than the other spatial dimensions in the domain. Also, the currents in the CNT are assumed to flow only in the axial direction ( $z$ -direction), according to the conductivity in (1).

All the composites considered in this paper are excited by a plane wave incident in the  $x$  direction normal to the dielectric, with the electric field polarized parallel to the CNT axes ( $z$ -axis) and with amplitude  $E_0$  (V/m) as shown in Fig. 1. In the unit cell in Fig. 1(b), each CNT will carry a different current  $I_n$ , where  $n$  is the index of the wire and there are  $1 \leq n \leq N$  wires in the unit cell. Since the incident wave is normal to the dielectric interface, the CNTs in each individual unit cell that are periodically linked, e.g., CNT A and B in Fig. 1(a), will carry the same current in comparison to the oblique incidence case where the current of periodically linked CNTs vary by a phase shift. An infinite CNT wire carrying a current  $I_n$ , centered at  $(x_n, y_n)$ , in an unbounded dielectric medium that has relative dielectric permittivity  $\epsilon_{rd}$ , will generate an electric field  $E_w$  at a location  $(x, y)$  given by [22], [23]

$$E_w(x, y) = -\frac{j\mu_0\omega I_n}{2s} \sum_{i=-\infty}^{+\infty} \exp[jP_s i(y - y_n)] \frac{\exp[-|x - x_n|U_i]}{U_i} \quad (5)$$

where  $U_i = [P_s^2 i^2 - k^2]^{1/2}$ ,  $P_s = 2\pi/s$ , and  $k = \omega\sqrt{\mu_0\epsilon_0\epsilon_{rd}}$ . The summation in (5) is over all the modes,  $i$ , which will only propagate when the frequency is large enough to make  $U_i$  purely imaginary. Each mode resembles a weighted plane wave propagating at a different angle. The dominant mode,  $i = 0$ , will propagate at all frequencies and it will be in the same direction as the incident wave. The consecutive modes at  $i = \pm 1$  will propagate when the wavelength  $\lambda$  is less than the periodicity  $s$  followed by the modes at  $i = \pm 2$ , which will propagate when the wavelength  $\lambda$  is less than  $(s/2)$  and so on. To solve for the

$N$  unknown currents  $I_n$  in the unit cell, the boundary conditions are enforced at an arbitrary point on the surface of each of the CNT wires in the unit cell in Fig. 1(b) because the radius of the CNT is much smaller than the incident wavelength and the other dimensions in the system. The boundary condition at this point  $(x_1 + b, y_1)$  on the surface of the  $n = 1$  CNT, can be expressed as follows:

$$E^{inc.} + E^{n=1} + E^{\forall n \neq 1} = Z_{cnt}^{filled} I_1 \quad (6)$$

where  $E^{inc.}$  is the complex field due to the normal incident plane wave,  $E^{n=1}$  is the complex self-scattered field by the  $n = 1$  wire itself, and  $E^{\forall n \neq 1}$  is the complex scattered field due to all the other CNTs ( $n = 2, 3, \dots, N$ ). The incident electric field  $E^{inc.}$ , which includes all the multiple reflection due to the dielectric slab, at a point on the surface of the CNT, for example  $(x_1 + b, y_1)$ , can be expressed as [22], [23]

$$E^{inc.} = \frac{E_0 t(0) \exp(-jk(x_1 + b))}{M(0)} + \frac{E_0 t(0) r(0) \exp(-jk(2d - x_1 - b))}{M(0)} \quad (7)$$

where  $r(0)$  and  $t(0)$  are the reflection and transmission coefficients, respectively, of mode  $i = 0$  calculated according to

$$r(i) = \frac{\sqrt{(iP_s)^2 - k^2} - \sqrt{(iP_s)^2 - k_0^2}}{\sqrt{(iP_s)^2 - k^2} + \sqrt{(iP_s)^2 - k_0^2}} \quad (8a)$$

$$t(i) = 1 - r(i) \quad (8b)$$

and the self-scattered field by the  $n = 1$  wire,  $E^{n=1}$  is shown in the equation at bottom of the page, and the scattered field due to all the other CNTs  $E^{\forall n \neq 1}$  at the surface of the CNT  $(x_1 + b, y_1)$  is shown in (10), at bottom of the page, where  $x'_1 = x_1 + b$  and  $M(i)$  accounts for the multiple reflections of mode  $i$  in the dielectric slab and can be evaluated as  $M(i) = 1 - r(i)^2 \exp(-2dU_i)$ ,  $r(i)$  is the reflection coefficient of mode  $i$  at the dielectric-air interface,  $t(i)$  is the transmission of mode  $i$  at the air-dielectric interface, and  $k_0 = \omega \sqrt{\mu_0 \epsilon_0}$ . Equation (6) represents 1 equation in  $N$  unknowns  $I_1, I_2, I_3, \dots, I_N$ . By applying the same boundary conditions as (6) on the other

wires  $n \neq 1$ ,  $N$  equations in  $N$  unknowns are achieved and they can be represented in the following matrix form:

$$[ZZ]_{N \times N} [I]_{N \times 1} = [V]_{N \times 1} \quad (11)$$

where  $[ZZ]$  is the impedance matrix,  $[I]$  is the vector containing the unknown currents  $I_1, I_2, \dots, I_N$ , and  $[V]_{N \times 1}$  is proportional to the incident fields [22], [23].

Upon solving (11), the unknown currents and all the reflected fields can be calculated at a point in free space  $(x_r, y_r)$ , where  $x_r < 0$ , by simple manipulation of (7)–(10) and the superposition of all the fields from the  $N$  CNTs as detailed in [22], [23].

## IV. NUMERICAL RESULTS

### A. Validation Using COMSOL

As a first step, the analytical model is numerically validated for a test case consisting of ten perfect electric conducting wires randomly dispersed in the dielectric slab, as shown in Fig. 3(a). The dielectric slab had a thickness  $d = 1$  mm, a relative dielectric permittivity  $\epsilon_{rd} = 2.5$ , and a periodicity  $s = 1$  mm in the  $y$ -direction. Each wire had a radius  $b = 0.001s = 1 \mu\text{m}$ . The analytical solution for the currents and fields is compared to the solution from the finite element (FEM) solver of the commercial multiphysics COMSOL<sup>1</sup> package [24].

Although the solutions to the above equations allow the calculation of the electromagnetic scattering at all angles and points in space, in this paper the reflected power will be used to summarize all this scattering information. Fig. 3(b) shows the reflected power versus the parameter  $s/\lambda_0$  where  $\lambda_0$  is the wavelength of the incident wave in free space. The reflected power is calculated by squaring the magnitude of the reflection amplitude, which is the ratio between the reflected field amplitude and the incident field amplitude in the far field. Fig. 3(b) shows that the reflected power from the 10 wires starts from a maximum of unity as the frequency approaches DC, or as the free space wavelength approaches infinity. The reflected power

<sup>1</sup>Certain commercial equipment, instruments, or materials are identified in this paper to foster understanding. Such identification does not imply recommendation or endorsement by the National Institute of Standards and Technology, nor does it imply that the materials or equipment identified are necessarily the best available for the purpose.

$$E^{n=1} = -\frac{j\mu\omega I_1}{2s} \sum_{i=-\infty}^{\infty} \frac{(\exp(-bU_i) + r(i) \exp(-U_i(2x_1 + b)) + r(i) \exp(-U_i(2d - 2x_1 - b)) + r(i)^2 \exp(-U_i(2d - b)))}{M(i)U_i} \quad (9)$$

$$E^{\forall n \neq 1} = -\sum_{n=2}^N \frac{j\mu\omega I_n}{2s} \sum_{i=-\infty}^{\infty} \frac{\exp(-jP_s i(y_1 - y_n))}{M(i)U_i} (\exp(-U_i|x'_1 - x_n|) + r(i) \exp(-U_i(x'_1 + x_n)) + r(i) \times \exp(-U_i(2d - x'_1 - x_n)) + r(i)^2 \exp(-U_i(2d - |x'_1 - x_n|))) \quad (10)$$

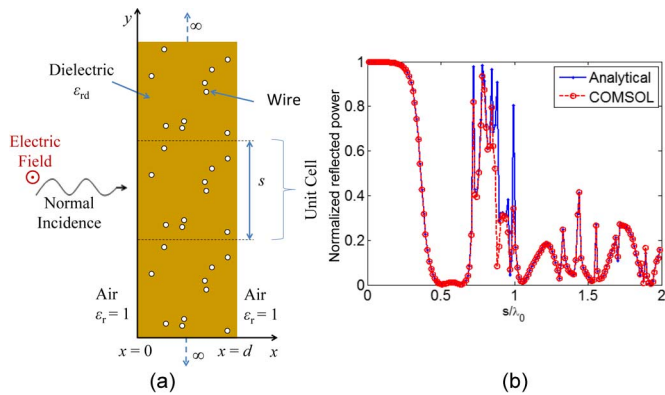


Fig. 3. (a) Configuration of the composite showing ten CNTs in each unit cell. (b) Reflected power from the composite in Fig. 2(a) using the analytical formulation and COMSOL for PEC wires.

then decreases to a first minimum at a frequency of 150 GHz which corresponds to a free space wavelength of 2 mm. The excellent agreement between the analytical and the FEM solution in Fig. 3(b) indicates the validity of our implementation of the analytical solution.

### B. Multiple Ordered CNT

The rest of this paper will only consider metallic CNTs that are (40, 40) armchair CNTs with a radius  $b = 2.7$  nm and using the conductivity values in (1). The CNTs were embedded in a dielectric slab with relative permittivity  $\epsilon_{rd} = 2.25$ . This permittivity value was chosen since it is comparable to that of common polymers such as polystyrene and poly(methyl methacrylate) that are frequently used in composites [25].

The main goal of this paper is to investigate how the randomness in the locations of multiple CNTs in a dielectric slab affects the electromagnetic response, and how this relation is affected by the separation between the CNTs and the properties of the dielectric slab. Therefore, in this section ordered CNTs are first simulated in order to quantify how CNT separation and dielectric slab properties affect the reflected power.

To study the effect of the separation between the CNTs on the reflected power, two CNTs with varying separation, embedded in air, will be investigated. The CNTs are separated horizontally ( $x$ ), vertically ( $y$ ), or diagonally ( $x$  and  $y$ ) as shown in Fig. 4(a)–(c), respectively.

Fig. 4(d)–(f) show the reflected power generated from the horizontal, vertical, and diagonal configuration from two CNTs embedded in a dielectric slab with a relative permittivity  $\epsilon_{rd} = 2.25$ . Silver filled CNT were chosen in Fig. 4 since it has the lowest impedance and therefore yields the highest reflected power. Also, a frequency of 3 THz is assumed, which is the highest frequency employed in this work and, therefore, will be the most sensitive to the CNT separation. The period is set to a value  $s = 33\mu\text{m}$  and the thickness of the dielectric slab is set to a value of  $d = \lambda_d/2 = 33\mu\text{m}$ . This thickness is chosen such that the reflection from the dielectric slab itself will be zero. In all cases considered in Fig. 4, the reflected power from a single CNT with half the effective impedance is shown as a dashed black line. In Fig. 4(d), where the CNT are separated horizontally, the reflected power is more than 5%

different from the power reflected from a CNT with half the impedance at a separation larger than  $2.4\mu\text{m}$  and the reflected power drops to a minimum at a separation of  $12.5\mu\text{m}$ . This is in comparison to separations of  $4.7\mu\text{m}$  and  $25\mu\text{m}$  when the CNT were embedded in air (result not shown). Therefore, the embedding of the CNTs in a dielectric slab reduces the minimum separation, by slightly more than the ratio between the refractive index of the dielectric slab and air, at which the two CNTs can be resolved into two distinct objects. Based on Fig. 4(d), any two CNT separated horizontally by less than  $2.4\mu\text{m}$  will appear to an incident wave of frequency 3 THz as one CNT with half the impedance. The physics behind Fig. 4(d) is similar to the Rayleigh criterion, where two objects need to be separated by a minimum distance, which is a function of the probing wavelength, before they can be resolved into two distinct objects.

In Fig. 4(e), the CNT are separated vertically. Comparing Fig. 4(e) with Fig. 4(d), it is clear that the reflected power is much less sensitive to the vertical separation than the horizontal separation. Also, since the CNT are periodic in the  $y$  direction the reflected power is symmetric around a separation of  $(s/2)$ . This is because, as the vertical separation increases beyond  $(s/2)$ , each CNT will get closer to the CNT in the next unit cell and the effective separation will start to decrease. The maximum reflected power is at the position where the CNT are evenly distributed vertically such that the separation between any two CNT is  $(s/2)$  as shown in Fig. 4(e).

When the CNT are separated diagonally, as shown in Fig. 4(f), the reflected power is very close to the horizontal separation shown in Fig. 4(d), since the reflected power is much more sensitive to the horizontal than the vertical CNT separation. Even though the reflected power from two CNTs shown in Fig. 4 is too small to be practically detected, the main conclusion from Fig. 4(d)–(f) is that if two CNTs are confined within a unit cell of  $s = 2.4\mu\text{m}$  and  $d = 2.4\mu\text{m}$ , no randomness in the reflected power is anticipated at 3 THz since the multiple CNTs will appear as one CNT with half the impedance regardless of their exact locations.

Now we investigate more complicated but still ordered CNT arrays using the circular arrangement of the CNTs shown in Fig. 5(a). In Fig. 5(b) 200 silver-filled CNTs are arranged in a circular arrangement of radius  $A$ , embedded in air with no dielectric slab at a frequency  $f = 1$  THz. In Fig. 5(b), the reflected power from the 200 CNTs is compared to the reflected power from a single fictitious wire with radius  $A$ , and an effective impedance  $Z_{\text{cyl}}^{\text{filled}}/200$ . It can be seen that for small values of  $A$ , the electromagnetic waves cannot penetrate the gaps between the CNTs because they are relatively close. This is why the CNTs will reflect almost the same power as the fictitious equivalent wire. The equivalence of the reflected power from the CNTs and the fictitious equivalent cylinder for small values of  $A$  has been previously employed in the numerical modeling of surfaces as wire grids [26].

As the radius  $A$  increases, the electromagnetic waves start to penetrate the gaps between the CNTs, the reflected power decreases and the CNTs can no longer be modeled as the fictitious equivalent wire. From Fig. 5(b) it can be seen that the reflected power from the 200 circularly arranged CNTs deviates

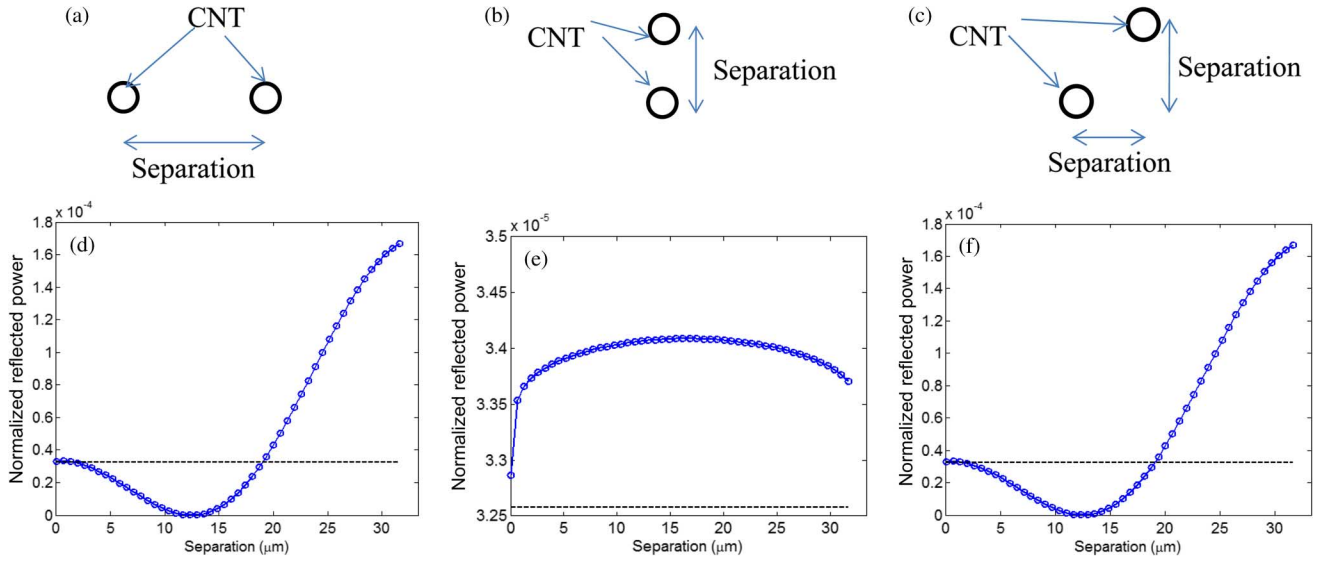


Fig. 4. (a) Horizontal ( $x$ ) separation configuration. (b) Vertical ( $y$ ) separation configuration. (c) Diagonal ( $x$  and  $y$ ) separation configuration. (d)–(f) Reflected power versus the separation between two CNTs, embedded in a  $\lambda/2$  dielectric slab, arranged in the horizontal, vertical, and diagonal configurations, respectively. In all cases, the frequency was 3 THz.

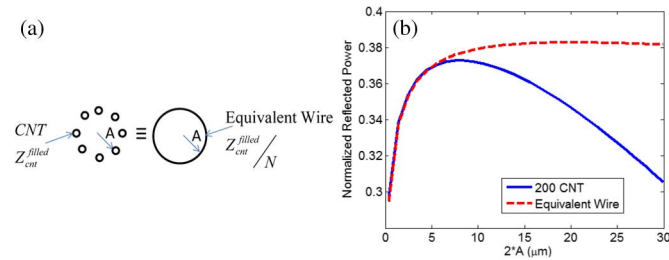


Fig. 5. (a) Circular CNT configuration and corresponding equivalent wire. (b) Reflected power from 200 circularly arranged CNT at  $f = 1$  THz.

from that of the fictitious equivalent wire by more than 5% at  $A_{5\%} = 7.4\mu\text{m}$  for the frequency  $f = 1$  THz. The radius  $A_{5\%}$  is almost linearly proportional to the wavelength with the slight deviation from linearity explained by the dispersive properties of the CNT and the filling silver.

The analysis in Fig. 5 again indicates roughly the minimum spatial dimensions required before variations in the reflected power can be achieved due to variations in the locations of the CNT. In other words, if 200 CNTs are randomly arranged within a circle of radius  $7.4\mu\text{m}$ , it is anticipated that the reflected power at 1 THz will be insensitive to their exact location since they will act as if they are a single wire with radius  $A = 7.4\mu\text{m}$  and  $(1/200)$  the conductivity of a single CNT. However, if they are displaced within a circle of larger radius their exact location will start to alter the reflected power.

### C. Multiple Randomly Centered CNT Wires

The spatial arrangement, orientation, and shapes of CNTs inside composites are typically random. In this model, we only investigate the effect of the randomness of the spatial positions of the CNTs in the  $x$ - $y$  plane, using more than one CNT.

Since the arrangement of the CNTs is random, if we average over many realizations there will be an average expected value along with a distribution for the reflected power. A sufficiently

large number of cases,  $M$ , of different unit cell realizations will serve to sufficiently map out the variations in the electromagnetic response and can be used to calculate the true average reflected power. To estimate the number of realizations needed for this task, the number of computed realizations is increased until the average appears to converge for each frequency investigated.

The average reflected power calculated using  $M = 800$  and  $M = 1600$  random realizations was very similar for all the number of CNTs considered in this paper. To quantify the variations of the reflected power from this average one can introduce the root means square (RMS) variations in the reflected power. For a function of frequency  $F(\omega)$ , one defines the RMS variations by

$$\text{RMS}(\omega) = \sqrt{\frac{1}{M} \sum_M (F(\omega) - \langle F(\omega) \rangle)^2} \quad (12)$$

where the angular brackets indicate an average over  $M$  realizations of the random unit cell. Close matching between the  $RMS$  calculated using  $M = 800$  and  $M = 1600$  realizations was also observed which indicates that  $M = 800$  different spatial realizations for the CNTs are sufficient to capture the main variations in the reflected power. All the following cases will therefore use  $M = 800$ .

In the following subsections, the variations in the reflected power for random arrays of CNTs with respect to the CNT number, the losses in the dielectric slab, the dimensions of the dielectric slab, the filling material inside the CNT, and the fabrication tolerances, are quantified.

1) *Number of CNTs*: We first study the variations in the reflected power for different CNT loadings. The dielectric slab is  $44\mu\text{m}$  thick with a relative dielectric permittivity  $\epsilon_{rd} = 2.25$  and  $s = 33\mu\text{m}$ . Fig. 6(a) shows the average reflected power for  $N = 1, 20, 100,$  and  $200$  silver filled CNTs. The CNT mass density is proportional to the number of CNTs in the unit

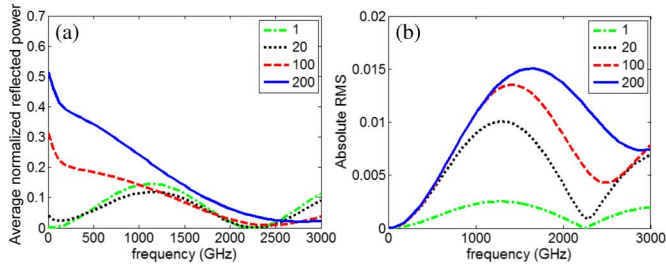


Fig. 6. (a) Average reflected power and (b) absolute RMS variation in the reflected power from 1, 20, 100, and 200 CNT composites.

cell of the composite. We use mass density in this model to better match to the quantity used in experiment and to show that the simple models considered in this paper have fairly realistic CNT mass fractions. To estimate the mass fraction,  $wf$ , in Fig. 6 we assume that the dielectric slab has the density of polystyrene,  $\rho_p = 1 \text{ g/cm}^3$ , and that silver has a density of  $\rho_s = 10 \text{ g/cm}^3$ . Therefore the mass fraction can be calculated using  $(N \cdot \pi b^2 \cdot \rho_s) / (s \cdot d \cdot \rho_p)$ . For  $N = 1, 20, 100$ , and  $200$  the corresponding mass fraction values are  $wf = 1.6 \times 10^{-5}\%$ ,  $3.2 \times 10^{-4}\%$ ,  $1.6 \times 10^{-3}\%$ , and  $3.2 \times 10^{-3}\%$ . Practical mass fractions to achieve percolation, termed percolation threshold, vary considerably as reported in the review by Bauhofer *et al.* [27]. In this review, the minimum and maximum percolation threshold were  $2 \times 10^{-3}\%$  and  $50\%$  mass fraction, respectively [27]. However, the review showed that in the vast majority of cases percolation was achieved at concentrations of  $0.1\%$  mass fraction or less [27]. The mass fraction at  $N = 200$  in Fig. 6 is comparable to the lower percolation thresholds reported in the literature [27]. Higher mass fractions are considered in the following Subsections.

Fig. 6(a) shows that at low frequencies,  $f < 100 \text{ GHz}$ , the reflected power increases with the number of CNTs,  $N$ . At higher frequencies, the reflected power from larger  $N$  values can be smaller than that from smaller  $N$  values. This can be explained by the fact that Fig. 6 presents the reflected power due to both the dielectric slab and the CNTs including any multiple reflections. At some frequencies, the CNTs enhance the reflected power from the dielectric slab and at other frequencies the CNTs diminish the reflected power from the dielectric slab. However, at low frequencies,  $f < 100 \text{ GHz}$ , the reflected power is predominantly due to the CNTs. Also, the minimum observed in the average reflected power for all  $N$  at around  $f = 2270 \text{ GHz}$  is due to the  $\lambda/2$  standing wave resonance in the dielectric slab. The effect of this minimum decreases as the number  $N$  increases and the response of the CNT dominates that of the dielectric slab, which is especially clear for the  $N = 200$  case in Fig. 6(a).

Fig. 6(b) shows that the RMS variations for the different numbers of CNTs increase with  $N$  at nearly all frequencies. This increase is due to the increase in the number of possible CNT spatial configurations as  $N$  increases. Fig. 6(b) shows that the variations in the reflected power are very small for low frequencies ( $< 50 \text{ GHz}$ ) and progressively start to increase as the frequency increases for all  $N$ . This is because at low frequencies the wavelength is sufficiently large that it cannot resolve the interelement distances between the CNTs. As the frequency increases, up to

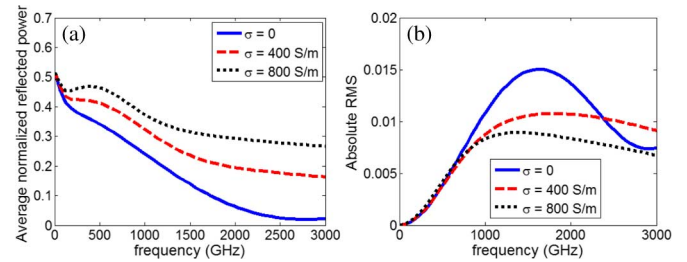


Fig. 7. (a) Average reflected power and (b) RMS variation in the reflected power from 200 CNT composites where the dielectric matrix had three possible conductivities.

a frequency of  $1500 \text{ GHz}$ , the variations increase as the wavelength decreases and the wavelength becomes small enough to resolve the locations of the CNTs in the unit cell. Therefore, the differences in the spatial positioning start to impact the reflected power as the frequency increases. Beyond  $1500 \text{ GHz}$ , the variations in the reflected power start to slowly decay to a minimum around  $f = 2270 \text{ GHz}$ , the frequency at which the empty dielectric slab will reflect zero power.

2) *Losses in Dielectric Slab*: CNT composites are fabricated from a large variety of polymers. Recently, there has been a great interest in CNT composites made from conducting polymers such as Polyaniline as shown in [28], [29]. Polyaniline has dc conductivity values in the order of  $333 \text{ S/m}$  [28], [29]. In the THz range, Tapia *et al.* recently showed that polyaniline emeraldine salt has a conductivity at  $290 \text{ K}$  that varies from  $280$ – $580 \text{ (S/m)}$  in the  $0.2$ – $1.2 \text{ THz}$  frequency range and that the conductivity increases with frequency and temperature [30]. To assess the effect of high losses in conducting polymers three different conductivities for the dielectric slab are investigated in Fig. 7:  $\sigma = 0 \text{ S/m}$ ,  $\sigma = 400 \text{ S/m}$ , and  $\sigma = 800 \text{ S/m}$ . Fig. 7 shows the impact of the losses in the dielectric slab on the variations in the reflected power, for  $N = 200$  and  $M = 800$ , with all other geometric and material parameters the same as in Fig. 6. The zero conductivity case is the same as the case presented in Fig. 6.

Fig. 7(a) shows that the average reflected power increases as the conductivity of the dielectric slab increases. This larger reflected power is primarily due to the losses in the dielectric slab increasing the mismatch between the composite and free space from where the incident wave is generated. Even though the average reflected power increases with the losses in the dielectric slab, as shown in Fig. 7(a), the RMS variations decrease with the losses as shown in Fig. 7(b). The losses in the dielectric slab attenuate the interactions between the CNTs, causing lower sensitivity to their geometric locations.

3) *Dimension of Dielectric Slab and CNT Filling Material*: The variations in the reflected power for dielectric slabs of two different dimensions,  $d = 11 \mu\text{m}$  and  $d = 44 \mu\text{m}$  are explored in Fig. 8. Also, three different filling cases were considered: 1) silver-filled CNT assuming the full bulk conductivity of silver; 2) silver-filled CNT assuming half the bulk conductivity of silver (termed *half\_silver*); and 3) empty CNT. A total of six cases are considered in Fig. 8, with  $N = 200$  CNTs,  $s = 33 \mu\text{m}$ , and slab relative dielectric permittivity  $\epsilon_{rd} = 2.25$ . In each of the six parts of Fig. 8, the thin blue line represents the reflected power from one realization, whereas the thick red

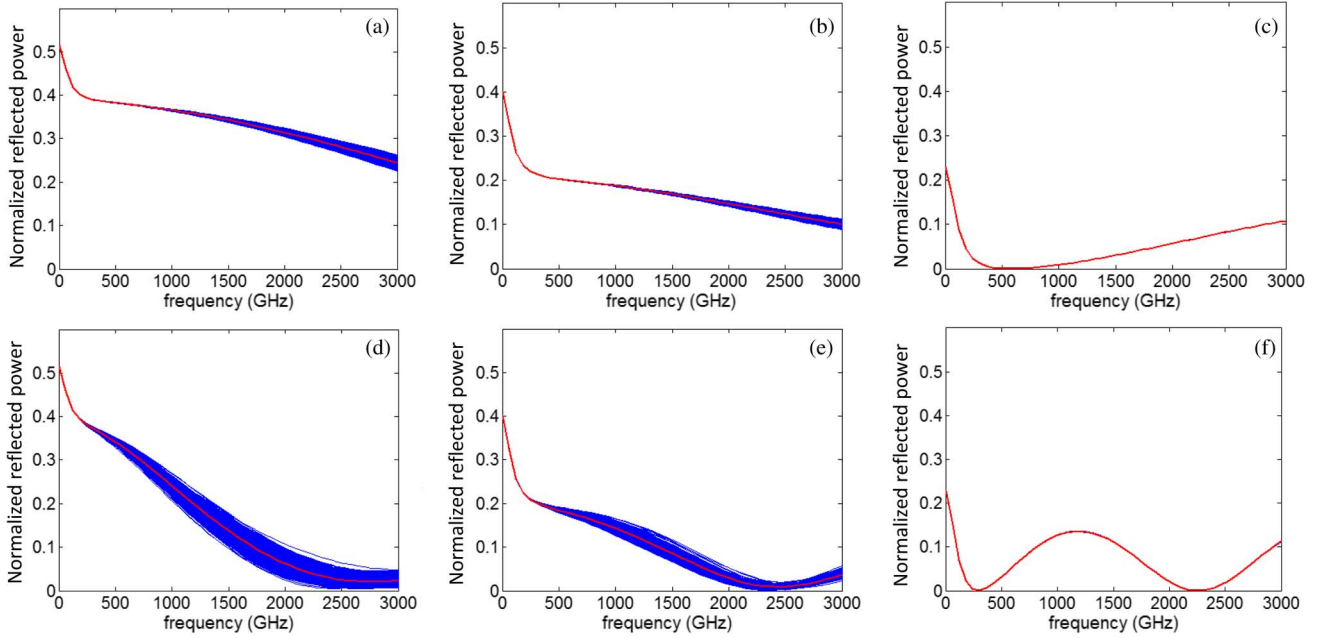


Fig. 8. Reflected power from  $M = 800$  realizations and the corresponding average reflected power for a composite composed of  $N = 200$  CNTs in the unit cell,  $s = 33\mu\text{m}$ , and dielectric slab thickness  $d = 11\mu\text{m}$ : (a) silver-filled CNTs; (b) *half\_silver* filled CNTs; and (c) empty CNTs. Slab thickness =  $44\mu\text{m}$ : (d) silver-filled CNTs; (e) *half\_silver* filled CNTs; and (f) empty CNTs.

line represents the corresponding average reflected power from all  $M = 800$  independent realizations.

Figs. 8(a)–(c) show the reflected power from a dielectric slab with a thickness  $d = 11\mu\text{m}$  for the cases of empty, *half\_silver*, and silver, respectively. Figs. 8(d)–(f) show the reflected power from a dielectric slab with a thickness  $d = 44\mu\text{m}$  for the same three cases. For the silver filled case, the CNT mass fraction is  $1.3 \times 10^{-2}\%$  and  $3.2 \times 10^{-3}\%$  for the dielectric slabs of thicknesses  $d = 11\mu\text{m}$  and  $d = 44\mu\text{m}$ , respectively. In experimental studies, this kind of realistic CNT mass fraction in epoxy resulted in percolation [27].

For the thinnest dielectric slab considered,  $d = 11\mu\text{m}$ , the spatial area where the CNT can be dispersed is smallest and, therefore, the variations in the reflected power are the smallest for each filler category, as shown in Fig. 8(a)–(c). These low variations in the reflected power in Fig. 8(a) versus the CNT spatial configuration can be explained using Figs. 4 and 5 in the previous section. Fig. 4(d) showed that any two silver filled CNTs, with a horizontal separation less than  $2.4\mu\text{m}$ , are effectively one CNT with half the impedance at 3 THz. Since in Fig. 8(a) the unit cell of the dielectric slab holds 200 CNTs and is only  $11\mu\text{m}$  thick, the average separations between the CNTs are much smaller than  $2.4\mu\text{m}$  and, therefore, the 200 CNTs will jointly appear similar to one CNT with  $Z_{\text{cnt}}^{\text{filled}}/200$  regardless of the exact positions of the CNTs. Using an alternative configuration, Fig. 5 showed that the CNTs in air need to be spread over a circle of radius larger than  $A = 7.4\mu\text{m}$  for the frequency  $f = 1\text{ THz}$ , for the reflected power to be different from one wire with  $Z_{\text{cnt}}^{\text{filled}}/200$ . These radii will scale approximately with the refractive index of the dielectric slab. This means that, for 1 THz for example, the CNT need to be spread over a circle of diameter larger than  $14.8/1.5 = 9.9\mu\text{m}$  for the reflected power to be sensitive to the exact location of the CNT. The width of the

dielectric slab in Fig. 8(a),  $d = 11\mu\text{m}$ , is almost the same as this diameter which explains why there is very little variation in the reflected power at frequencies less than 1 THz. Fig. 8(b) shows similar behavior to Fig. 8(a) except that it exhibits slightly lower variations at all frequencies due to the lower conductivity of the *half\_silver* filling.

For the empty CNTs, Fig. 8(c) shows no variations in the reflected power for a dielectric slab of thickness  $d = 11\mu\text{m}$ . For such a thin slab, Fig. 8(a) and (b) showed that a frequency higher than 1 THz is needed for the reflected power to be sensitive to the exact CNT location. However, the impedance of empty CNTs rises steeply at frequencies higher than 50 GHz, as was illustrated in Fig. 2. Therefore, at frequencies higher than 1 THz the effect of the CNT vanishes completely and in turn the variations due to the exact position of the CNTs also vanish. Beyond 50 GHz, the response of the CNT vanishes all together and the reflection is primarily due to the dielectric and this is why it will start to increase to follow the standing wave pattern characteristic of a dielectric slab in air. However, for the cases of silver and *half\_silver* filled CNTs, variations persisted at frequencies higher than 1 THz since silver maintains its conductivity at these higher frequencies, so that there still was a small but nonzero variation in the reflected power due to the exact spatial position of the CNTs, as shown in Fig. 8(a) and (b).

When the thickness of the dielectric slab increases to  $44\mu\text{m}$ , the variations in the reflected power increase as shown in Fig. 8(d) and (e). This is because the dielectric slab is thicker in this case and the CNT are dispersed over a spatially larger domain in comparison to the frequency of interest.

After quantifying the variations in the reflected power, it is interesting to identify which kinds of CNT locations lead to the maximum, minimum, or other selected values of reflected power at all frequencies. Considering the  $44\mu\text{m}$  thick dielec-

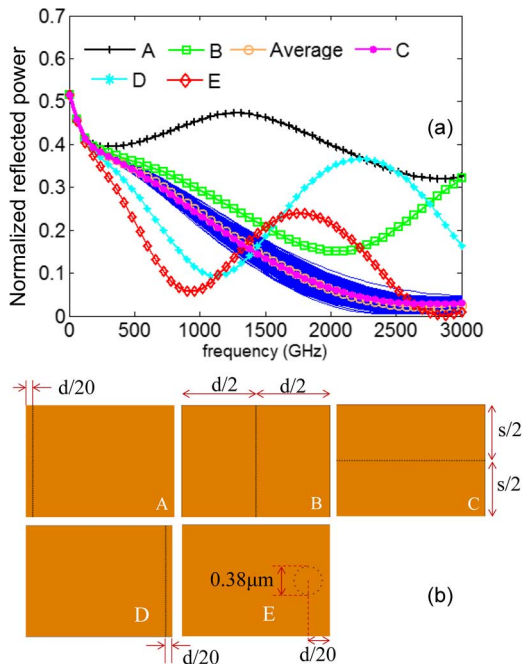


Fig. 9. (a) Reflected power for five different CNT spatial realizations. (b) Corresponding five unit cells each containing 200 CNTs. For clarity, not all the 200 CNT are shown in each case. For all cases  $s = 33 \mu\text{m}$  and  $d = 44 \mu\text{m}$ .

tric slab, Fig. 9 shows 5 different spatial distributions of the  $N = 200$  silver-filled CNTs and the corresponding reflected power. The bulk conductivity of silver is assumed in Fig. 9. The properties of the dielectric slab and the CNT arrays in Fig. 9 are the same as those in Fig. 8(d). These five special cases appear to encase the averaged 800 random distributions, which are copied to Fig. 9 from Fig. 8(d) for easier comparison.

The five cases shown in Fig. 9 are arranged in descending order of reflected power at low frequencies  $f < 1$  THz. In this frequency range, the five cases show that when the CNTs get closer to the interface that is closest to the incident wave's first interface ( $x = 0$ ), the reflected power increases. When the CNTs move away this interface, the reflected power decreases. In configuration A, the CNTs are vertically arranged and moved closest to the interface, which yields the maximum reflected power. This special case is significantly higher than all the 800 random cases in Fig. 8(d). However, if the number of random cases is progressively increased configuration A will be eventually achieved, although it is obviously of very low probability. When the CNTs are arranged vertically but moved to the middle of the dielectric slab, as shown in configuration B, the reflected power drops as seen in the green-square curve. Therefore, the dielectric slab acts as a buffer between free space and the CNT and the larger the portion of the dielectric slab between the CNT and free space the lower the value of the reflected power. When the CNTs are arranged horizontally, as shown in configuration C in Fig. 9, the reflected power shown in magenta-dotted is achieved. This reflected power is very close to the average reflected power from the random 800 CNT configurations shown in orange-circle in Fig. 9. The minimum reflected power is achieved when the CNTs are arranged in a very tight circular configuration of diameter  $0.38 \mu\text{m}$  and moved far away from the left interface as shown in configuration E in Fig. 9.

The five configurations yielded qualitatively similar behavior for unit cells with different values of  $s$  and  $d$ .

For frequencies larger than 1 THz, the order of the reflected power from the five cases becomes intermingled. This is due to the fact that Fig. 9 shows the convoluted reflected power due to both the dielectric slab and the CNTs. For low frequencies, the reflected power is due to mainly the CNTs and, therefore, the relation of the reflected power versus the CNT configuration is clear. However, for larger frequencies the CNTs enhance the reflected power at some frequencies and diminish the reflected power at other frequencies.

It is important to emphasize that in practical composites, it is challenging to achieve the precise configurations shown in Fig. 9(b). However, the specific spatial realizations shown in Fig. 9(b) are only presented to explain the general trend in the reflected power as the spatial realization of the CNTs is varied. What can be concluded from configuration A, for practical composites, is that the reflected power from a composite will increase if the random CNTs in a composite are moved closer to the interface instead of being uniformly distributed. One practical reason where the CNTs can accumulate near the interface of a composite was shown recently in [31]. In [31], Petersen *et al.* showed that when a carbon nanotube epoxy composite is exposed to UV light, the epoxy degrades which led to the accumulation of the CNTs on the interface exposed to the light. Based on the results in Fig. 9, it is anticipated that the reflected power from a UV exposed composite will be larger than the reflected power from an unexposed composite. Another prediction based on Fig. 9(b) can be obtained from configuration E where the CNTs are arranged in a very tight circular configuration. In a practical composite, it is hard to arrange the CNTs in a perfect circle. However, what can be concluded from configuration E is that if the CNTs in a composite are dispersed into very concentrated and isolated aggregates then the reflected power is anticipated to be smaller than when the CNTs are uniformly distributed throughout the dielectric slab.

A final dimension to consider is the period in the  $y$ -direction,  $s$ . When the  $s$  value is reduced from the values presented in Fig. 8, the effective mass fractions of the CNTs increases and, therefore, the exact location of the CNTs has a larger effect on the reflected power. This will lead to more variations in the reflected power than in the more dilute cases presented in Fig. 8.

4) *Nonidentical CNT*: In the previous sections, the CNTs in each configuration were all identical. That is, they were either all silver filled or all empty. However, in real composites all the CNTs will not be identical and on average only a fraction of CNTs will be silver filled. The model can be adapted to simulate nonidentical CNTs by assigning different impedances to each CNT. Therefore, the silver filled CNTs will be assigned impedance  $Z_{\text{cnt}}^{\text{filled}}$  as in (3) whereas empty CNTs will be assigned impedance  $Z_{\text{cnt}}^{\text{empty}}$  as in (2).

In Fig. 10, a composite with 200 nonidentical CNT is simulated. Fig. 10(a) shows the reflected power due to  $M = 800$  different locations and the corresponding average power. In addition to varying the locations of the CNTs, the number of silver filled CNT was varied, in each of the  $M = 800$  cases, according to a Gaussian distribution with a mean of 100 CNT and a standard deviation of  $\pm 20$  CNT. The dielectric slab had a thickness

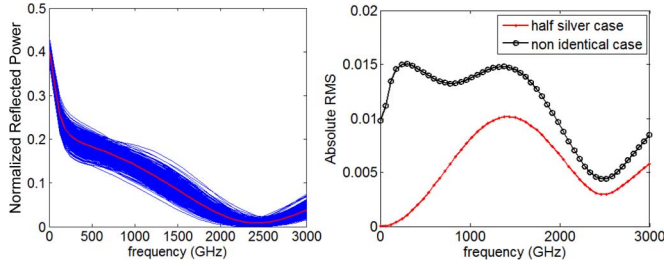


Fig. 10. (a) Reflected power from  $M = 800$  realizations and the corresponding average reflected power for a composite composed of  $N = 200$  nonidentical CNTs (some filled with silver and some not) (b) RMS variations in the reflected power from 200 nonidentical CNT and from 200 identical *half\_silver* CNT.

$d = 44\mu\text{m}$  and the period in the  $y$ -direction  $s = 33\mu\text{m}$  similar to the configuration of Fig. 8(d)–(f). For the silver filled CNTs, the bulk conductivity of silver was assigned.

The average reflected power in Fig. 10(a) is the same as the average reflected power in the *half\_silver* case in Fig. 8(e). This is anticipated since on average 50% of the CNT were silver filled in Fig. 10(a). However, comparing Fig. 10(a) with Fig. 8(e) it is clear that the variation in the reflected power due to the non-identical CNT case is more than the *half\_silver* case. This is also demonstrated in Fig. 10(b) which shows that the RMS variations due to the nonidentical CNTs case are more than the *half\_silver* case at all frequencies. This increase in the variation is due to the convolutions of two random factors which are the locations of the CNT and whether they are filled with silver or not.

At low frequencies,  $f < 100$  GHz, the *half\_silver* case showed almost zero RMS whereas the nonidentical case showed nonzero RMS in this frequency range. This shows that the RMS in this frequency range is not due to the variations in the locations of the CNT since the wavelength at this frequency range is too large to resolve the exact locations of the CNTs inside the slab. However, the nonzero RMS in this frequency range is due to the variation in the number of silver filled CNTs. At low frequencies, the maximum reflected power in Fig. 10(a) originated from the cases which had the most silver filled CNT whereas the minimum reflected power in Fig. 10(a) originated from the cases which had the fewest silver filled CNT.

5) *Fabrication Tolerances*: Based on all the previous results, we can now apply the model to estimate the variations in the reflected power due to fabrication tolerances. Fig. 11(a) shows a composite where the  $N = 200$  silver filled CNT are intended to be lined up perfectly at constant  $x$  at the center of the dielectric slab with  $d = 44\mu\text{m}$  and  $s = 33\mu\text{m}$ . The ideal alignment in Fig. 11(a) corresponds to configuration B in Fig. 9. In any manufacturing process, fabrication tolerances can lead to misalignments in the locations of the CNT as seen in one example in Fig. 11(b). Given an estimate of the fabrication tolerances in the position of the CNTs, the corresponding variations in the reflected power can be estimated. For example, the tolerance in the  $y$ -direction is assumed to be  $\pm 0.002s$  and three different tolerances in the  $x$ -direction are assumed,  $\pm 0.05d$ ,  $\pm 0.08d$ , and  $\pm 0.1d$ , around the ideal aligned configuration in Fig. 11(a). Therefore, each CNT will be randomly placed, with

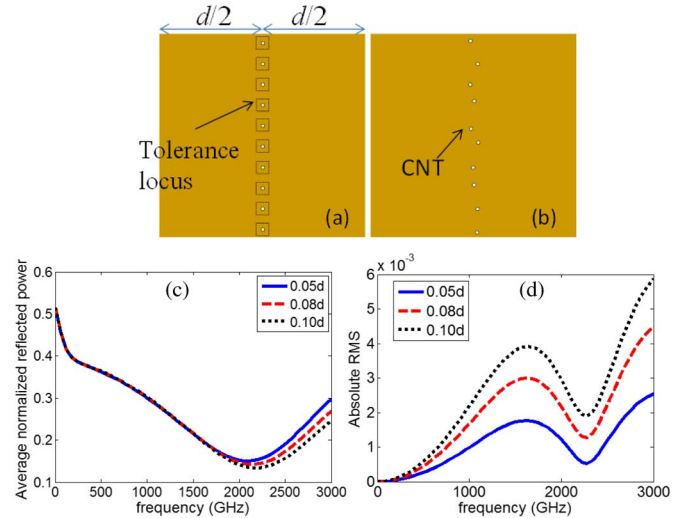


Fig. 11. (a) Ideal designed CNT positions (only 10 CNT out of the 200 CNT were shown for this illustration), (b) example of a misaligned CNT array due to fabrication tolerance, (c) average reflected power from 800 realizations of misaligned CNTs, and (d) absolute RMS variations calculated from the previous 800 misaligned CNTs.

equal probability, anywhere within a rectangle centered on each designed position similar to the sketch in Fig. 11(a).

The average reflected power from  $M = 800$  cases and the corresponding absolute RMS are shown in Fig. 11(c) and (d), respectively. The average reflected power varies only slightly at frequencies higher than 2 THz. As the tolerance in the  $x$  direction increases, the average reflected power decreases indicating that the perfect vertical alignment at the center of the dielectric slab yields the maximum reflection. As would be expected, the absolute RMS variations increase as the tolerance increases, as shown in Fig. 11(d). In Fig. 4(d), when two CNT were separated horizontally by less than  $2.4\mu\text{m}$ , the reflected power was less than 5% different from the power reflected from a CNT with half the impedance. The first tolerance value in the  $x$ -direction presented in Fig. 11 correspond to  $\pm 0.05d = \pm 2.22\mu\text{m}$  which is smaller than  $2.4\mu\text{m}$  and therefore minimal variations were seen for this tolerance value in Fig. 11(d). However, as the tolerance value in the  $x$ -direction increased to  $\pm 0.08d = \pm 3.55\mu\text{m}$  and  $\pm 0.1d = \pm 4.44\mu\text{m}$ , which is larger than  $2.4\mu\text{m}$ , noticeable variations occurred in the reflected power as shown in Fig. 11(d).

## V. CONCLUSIONS AND FUTURE WORK

A model was developed to simulate the electromagnetic scattering from CNT composites. The new aspects of the model, in contrast to previous models, were that the CNT, which were modelled as parallel, infinite wires, were embedded in a dielectric slab with a finite thickness in the  $x$ -direction and the center locations of the CNT were varied randomly inside a unit cell of the slab. The model showed that the reflected power from the composite was sensitive to the exact locations of the CNTs and to their locations with respect to the interfaces of the dielectric slab. The random geometry of the CNTs in the model generated

a random electromagnetic reflection response, which was computed and characterized statistically.

The model showed that composites with metal-filled CNTs exhibit larger variation in the electromagnetic scattering than do composites with unfilled CNTs. This is attributed to the fact that metals retain their conductivity to higher frequencies in comparison to unfilled CNTs. Increasing the CNT density increases the variations in the electromagnetic scattering, and increasing the losses of the dielectric slab decreases the variations in the electromagnetic scattering. Ideas developed for the scattering of pairs or ordered clusters of CNTs were used to help explain the effect of these parameters and random CNT placement geometry on the variability of the electromagnetic scattering response. These results were applied to a fabrication tolerance problem, where the effect of random errors in CNT placement during manufacturing on electromagnetic scattering was quantitatively predicted.

Several effective medium approaches have been previously proposed in the literature to simplify the modeling of similar composites such as carbon fiber composites [32]. One particular effective medium approach has modeled the carbon fiber composite as multiple homogeneous and inhomogeneous layers [32]. The analytical model presented in this work, can act as a guide to optimize the number of homogeneous and inhomogeneous layers required to accurately simulate the CNT composites similar to the approach in [32].

This analytical work on CNT arrays embedded in a dielectric slab will also provide a guide to the development of more realistic models of CNT composites, where the CNTs are random in all three dimensions as well as random in shape. The effect of random shape on the electromagnetic properties of individual CNTs is being studied at present and results will be presented in a future paper.

## REFERENCES

- [1] M. De Volder, S. Tawfick, R. Baughman, and A. Hart, "Carbon nanotubes: Present and future commercial applications," *Science*, vol. 339, pp. 535–539, 2013.
- [2] A. Mehdipour, I. Rosca, A. Sebak, C. Trueman, and S. Hoa, "Carbon nanotube composites for wideband millimeter-wave antenna applications," *IEEE Trans. Antennas Propag.*, vol. 59, no. 10, pp. 3572–2578, Oct. 2011.
- [3] C. Ren, Q. Gong, L. Guo, X. Zhao, and J. Liang, "Analyses of reinforcing effects of *in situ* grown CNTs on carbon fibre fabric/epoxy composites at micro- and macroscale," *Micro Nano Lett.*, vol. 7, no. 3, pp. 240–243, 2012.
- [4] S. Mikki and A. Kishk, "Theory of optical scattering by carbon nanotubes," *Microw. Opt. Technol. Lett.*, vol. 49, pp. 2360–2364, 2007.
- [5] J. Berres and G. Hanson, "Multiwall carbon nanotubes at RF-THz frequencies: Scattering, shielding, effective conductivity, power dissipation," *IEEE Trans. Antennas Propag.*, vol. 59, no. 8, pp. 3098–3103, Aug. 2011.
- [6] I. Nefedov, "Electromagnetic waves propagating in a periodic array of parallel metallic carbon nanotubes," *Phys. Rev. B*, vol. 82, p. 155423, 2010.
- [7] G. Hanson, "Fundamental transmitting properties of carbon nanotube antennas," *IEEE Trans. Antennas Propag.*, vol. 53, no. 11, pp. 3426–3435, Nov. 2005.
- [8] J. Hao and G. Hanson, "Electromagnetic scattering from finite-length metallic carbon nanotubes in the lower IR bands," *Phys. Rev. B*, vol. 74, p. 035119, 2006.
- [9] J. Hao and G. Hanson, "Optical scattering from a planar array of finite-length metallic carbon nanotubes," *Phys. Rev. B*, vol. 75, p. 165416, 2007.
- [10] S. Mikki and A. Kishk, "Mean-field electrodynamic theory of aligned carbon nanotube composites," *IEEE Trans. Antennas Propag.*, vol. 57, no. 5, pp. 1412–1419, May 2009.
- [11] A. Sotiropoulos, I. Plegas, S. Koulouridis, and H. Anastassiou, "Scattering properties of carbon nanotube arrays," *IEEE Trans. Electromagn. Compat.*, vol. 54, no. 1, pp. 110–117, Feb. 2012.
- [12] R. Zhang, Y. Zhang, Q. Zhang, H. Xie, W. Qian, and F. Wei, "Growth of half-meter long carbon nanotubes based on Schulz-Flory distribution," *ACS Nano*, vol. 7, no. 7, pp. 6156–6161, 2013.
- [13] I. Liberal, I. Ederra, C. Gómez-Polo, A. Labrador, J. Pérez-Landazábal, and R. Gonzalo, "A comprehensive analysis of the absorption spectrum of conducting ferromagnetic wires," *IEEE Trans. Microw. Theory Techn.*, vol. 60, no. 7, pp. 2055–2065, Jul. 2012.
- [14] A. Hassan and E. Garboczi, "Electromagnetic scattering from a carbon nanotube array embedded in a dielectric slab," presented at the Proc. 40th Annu. Rev. Progr. Quantitative Nondestructive Eval. Conf., Baltimore, MD, USA, 2013.
- [15] G. Slepuyan, S. Maksimenko, A. Lakhtakia, O. Yevtushenko, and A. V. Gusakov, "Electrodynamics of carbon nanotubes: Dynamic conductivity, impedance boundary conditions, surface wave propagation," *Phys. Rev. B*, vol. 60, p. 17136, 1999.
- [16] G. Slepuyan, M. Shuba, S. Maksimenko, C. Thomsen, and A. Lakhtakia, "Terahertz conductivity peak in composite materials containing carbon nanotubes: Theory and interpretation of experiment," *Phys. Rev. B*, vol. 81, no. 205423, 2010.
- [17] G. Hanson, "Radiation efficiency of nano-radius dipole antennas in the microwave and far-infrared regimes," *IEEE Antennas Propag. Mag.*, vol. 50, no. 3, pp. 66–77, Jun. 2008.
- [18] C. A. Grimes, E. C. Dickey, C. Mungle, K. G. Ong, and D. Qian, "Effect of purification of the electrical conductivity and complex permittivity of multiwall carbon nanotubes," *J. Appl. Phys.*, vol. 90, no. 8, pp. 4134–4137, 2001.
- [19] U. Weissker, S. Hampel, A. Leonhardt, and B. Büchner, "Carbon nanotubes filled with ferromagnetic materials," *Materials*, vol. 3, no. 8, pp. 4387–4427, 2010.
- [20] M. Ordal, R. Bell, R. Alexander, Jr., L. Long, and M. Querry, "Optical properties of fourteen metals in the infrared and far infrared: Al, Co, Cu, Au, Fe, Pb, Mo, Ni, Pd, Pt, Ag, Ti, V, W," *Appl. Opt.*, vol. 24, no. 24, pp. 4493–4499, 1985.
- [21] J. Park, T. Wang, H. Kim, and Y. Doh, "Experimental and numerical study of the electrical anisotropy in unidirectional carbon-fiber-reinforced polymer composites," *Smart Mater. Struct.*, vol. 16, pp. 57–66, 2007.
- [22] J. R. Wait, "The impedance of a wire grid parallel to a dielectric interface," *IRE Trans. Microw. Theory Techn.*, vol. 5, no. 2, pp. 99–102, 1957.
- [23] J. R. Wait, "Electromagnetic scattering from a wire grid parallel to a planar stratified medium," *IEEE Trans. Antennas Propag.*, vol. AP-20, no. 5, pp. 672–675, Sep. 1972.
- [24] Comsol. (December 2013) [Online]. Available: <http://www.comsol.com>
- [25] H. Peng and X. Sun, "Highly aligned carbon nanotube/polymer composites with much improved electrical conductivities," *Chem. Phys. Lett.*, vol. 471, no. 1–3, pp. 103–105, 2009.
- [26] A. Ludwig, "Wire grid modeling of surfaces," *IEEE Trans. Antennas Propag.*, vol. AP-35, no. 9, pp. 1045–1048, Sep. 1987.
- [27] W. Bauhofer and J. Kovacs, "A review and analysis of electrical percolation in carbon nanotube polymer composites," *Composites Sci. Technol.*, vol. 69, no. 10, pp. 1486–1498, 2009.
- [28] H. Zengin, W. Zhou, J. Jin, R. Czerw, D. Smith, Jr., L. Echegoyen, D. Carroll, S. Foulger, and J. Ballato, "Carbon nanotube doped polyaniline," *Adv. Mater.*, vol. 14, no. 20, pp. 1480–1483, 2002.
- [29] M. Cochet, W. Maser, A. Benito, M. Callejas, M. Martínez, J. Benoit, J. Schreiber, and O. Chauvet, "Synthesis of a new polyaniline/nanotube composite: "in-situ" polymerisation and charge transfer through site-selective interaction," *Chem. Commun.*, vol. 37, no. 16, pp. 1450–1451, 2001.
- [30] A. Tapia and K. Tominaga, "Conduction in polyaniline emeraldine salt in the terahertz region: A temperature dependence study," *Chem. Phys. Lett.*, vol. 598, pp. 39–42, 2014.
- [31] E. Petersen, T. Lam, J. Gorham, K. Scott, C. Long, D. Stanley, R. Sharma, J. Liddle, B. Pellegrin, and T. Nguyen, "Methods to assess the impact of UV irradiation on the surface chemistry and structure of multiwall carbon nanotube epoxy nanocomposites," *Carbon*, vol. 69, pp. 194–205, 2014.
- [32] C. L. Holloway, M. S. Sarto, and M. Johansson, "Analyzing carbon-fiber composite materials with equivalent-layer models," *IEEE Trans. Electromagn. Compat.*, vol. 47, no. 4, pp. 833–844, Nov. 2005.



**Ahmed M. Hassan** (S'07–M'12) received the B.Sc. degree (with highest honors) and M.Sc. degree from Cairo University, Cairo, Egypt, in 2004 and 2006, respectively, both in electronics and communications engineering, and the Ph.D. degree in electrical engineering from the University of Arkansas, Fayetteville, AR, USA, in 2010.

From 2004 to 2006, he was a Teaching Assistant at Cairo University, where he was also an Assistant Lecturer during 2006. From 2007 to 2010, he was a Teaching and Research Assistant in the Department of Electrical Engineering at the University of Arkansas. From 2011 to 2012, he was a Postdoctoral Fellow in the Computational Electromagnetics Group at the University of Arkansas. Currently, he is a Guest Researcher at the National Institute of Standards and Technology, Gaithersburg, MD, USA. His current research interests include nanoelectromagnetics, bioelectromagnetics, inverse scattering algorithms, experimental microwave imaging, terahertz imaging, and metamaterials.

Dr. Hassan was the recipient of the Doctoral Academy Fellowship at the University of Arkansas and the Outstanding Poster Award in the 2014 21st Annual NIST Sigma Xi Postdoctoral Poster Presentation.



**Edward J. Garboczi** received the B.S. degree in physics (with highest honors) and the Ph.D. degree in condensed matter physics (theory) from Michigan State University, East Lansing, MI, USA, in 1980 and 1985, respectively.

From 1985 to 1988, he was a Research Physicist in Armstrong World Industries, Inc. in Lancaster, PA, USA. From 1988 to 2014, he was a Physicist, Group Leader, and finally a Fellow at the National Institute of Standards and Technology (NIST), Materials and Structural Systems Division, Gaithersburg, MD, USA. In 2014, he moved to the NIST Boulder, CO, USA site in the Division of Applied Chemicals and Materials Division. His research interests include computational materials science, porous materials, electrical properties of nanocomposites, and 3-D particle shape analysis of a wide range of particles including gravel, sand, cement, chemical explosives, lunar soil, and metal powder for additive manufacturing.

Dr. Garboczi is a Fellow of the American Concrete Institute (ACI), the American Ceramic Society (ACerS), and is the recipient of the ACI Robert E. Philleo award, the ACerS Della Roy Lecture Award, the ACers Edward C. Henry Best Paper Award (Electronics Division), and a Silver Medal from the Department of Commerce for the creation of the Virtual Cement and Concrete Testing Laboratory.